

Simulation Study on the Optimization of Photon Energy Delivered to the Prefrontal Cortex in Low-Level-Light Therapy Using Red to Near-Infrared Light

Li-Da Huang, *Senior Member, IEEE*, Tzu-Chia Kao, Kung-Bin Sung[✉], and Jacob A. Abraham[✉], *Fellow, IEEE*

Abstract—Brain functions have been proved to be affected by external stimuli. Low-Level-Light Therapy (LLLT) using near-infrared photons is one of the effective ways to modulate the hemodynamic activities in the brain. However, the biphasic hormetic dose-response where bioenergetics are stimulated at a low dose and inhibited at a high dose is well observed in all photon stimulations. The amount of photon energy delivered to the brain are affected by the wavelength as well as the multilayered head structure with variations of optical parameters (OPs). A real 3D volume head model is built for each participant in this study, and the boundary conditions of each OP in each layer is considered. The Monte Carlo simulation with wavelengths ranging from 650 nm to 1064 nm is implemented to investigate the energy delivered to the brain under different radiation profiles. Results show that 1064-nm photons penetrate deeper than 810-nm photons except for scalp absorption at the lower bound due to low melanin content. Collimated-beam radiation is better than diverging-beam due to a more uniform intensity distribution at the scalp surface. Further research to optimize LLLT dosage for each individual is imperative due to the high inter-person variability in structure and OPs.

Index Terms—Biomedical applications of optical radiation, dosimetry, Monte Carlo methods.

I. INTRODUCTION

THE deterioration of the brain function during the aging process or the healing from a trauma is always the key factor of the quality of life. Could the brain function be enhanced?

Manuscript received October 10, 2020; revised January 11, 2021; accepted January 11, 2021. Date of publication January 14, 2021; date of current version March 24, 2021. This work was supported by the Ministry of Science and Technology in Taiwan under Grant 108-2221-E-002-075-MY3. (*Corresponding author: Kung-Bin Sung*.)

Li-Da Huang is with the University of Texas at Austin, Austin, TX 78752 USA, and also with the CytonSys Inc, Austin, TX 78752 USA (e-mail: lida@cytonsys.com).

Tzu-Chia Kao is with the Graduate Institute of Biomedical Electronics and Bioinformatics, National Taiwan University, Taipei 10617, Taiwan (e-mail: r07945005@ntu.edu.tw).

Kung-Bin Sung is with the Graduate Institute of Biomedical Electronics and Bioinformatics, the Department of Electrical Engineering, and the Molecular Imaging Center at National Taiwan University, Taipei 10617, Taiwan (e-mail: kbsung@ntu.edu.tw).

Jacob A. Abraham is with the Department of Electrical and Computer Engineering at the University of Texas at Austin, Austin, TX 78752 USA (e-mail: jaa@cerc.utexas.edu).

This article has supplementary material provided by the authors and color versions of one or more figures available at <https://doi.org/10.1109/JSTQE.2021.3051671>.

Digital Object Identifier 10.1109/JSTQE.2021.3051671

Or could the brain deterioration due to aging be delayed? That has been a most studied topic in the areas of physical medicine and rehabilitation [1].

Among the non-invasive treatments, low-level-light therapy (LLLT) has increasingly become a mainstream modality [1]. Although at first LLLT has been used mainly for wound healing and pain relief, the medical applications of LLLT have broadened to include diseases such as stroke, myocardial infarction, and degenerative or traumatic brain disorders [2]–[8]. In addition, upconversion nano-particles that are excited at NIR and emit blue light have been fabricated and demonstrated to trigger neural activations in the deep brain through optogenetics [9].

LLLT uses low-powered laser light in the range of 1–1000 mW, at wavelengths ranging from 632 nm to 1064 nm, to stimulate a biological response [1]. LLLT is different from other external stimuli such as heat, sound, or vibration by that LLLT acts through inducing a photochemical reaction within the cell, a process referred to as biostimulation or photobiomodulation [1]. There are many different mechanisms of the photon to affect the bio tissue or the metabolic system. For the LLLT on the brain, its basic mechanism is to excite the cytochrome c oxidase (CCO), which is a mitochondrial respiratory enzyme. The CCO is a photo acceptor that could be excited at 620 nm to 1150 nm. The effects of photobiomodulation could be observed through hemodynamics such as the increase of the oxygenated hemoglobin concentration, the decrease of the deoxygenated hemoglobin concentration, and the improvement of cerebral oxygenation (i.e., the difference of the oxygenated hemoglobin and the deoxygenated hemoglobin concentrations) [3], [6].

The first controlled study [10] demonstrating the beneficial effects of LLLT on cognitive and emotional functions in humans shows that LLLT could be used as a non-invasive and efficacious approach to increase brain functions. In [12], LLLT is further shown how it is related to electroencephalography (EEG) and how it enhances the cognitive functions for the senior people. More and more experiments and promising results [2]–[8] indicate that LLLT using near-infrared light is an effective non-invasive approach to enhance the brain functions.

However, because the brain tissue such as the grey matter (GM) is below the scalp, skull, among the cerebrospinal fluid (CSF), and with the gyri folding the tissues on the surface

to increase the area for the billions of the neurons and the connections, the brain model fundamentally is a multi-layer structure with various optical parameters. Therefore, in the past decades, researchers have faced the challenge to find the proper wavelength, the power and the exposure time to achieve consistent results. In [11], the 810 nm wavelength is considered to deliver the most energy to the target tissues. In [10] and [12], 1064 nm is used to show the enhanced cognitive functions in various human trials.

In the literature [11]–[14], there has been an continuing argument about what the best setting of the wavelengths, power, and the exposure time are. Several computational model and simulation results have been presented. However, all of these results are incomplete due to the three-dimensional (3D) volume head models being inaccurate, or the optical parameters settings being biased to a certain range. Therefore, the concluded best setting of LLLT varied quite substantially. In this research, we studied a wide range of wavelengths and considered the optical parameters for all the boundary conditions (i.e., upper bound and lower bound) at wavelengths ranging from 650 nm to 1064 nm. In addition, we built the 3D volume head model for each participant in order to study the variation among them. Our results indicate that the customized setting for each person is very important to achieve the optimized result. That also resolves why there is an unconcluded discussion for the best settings for all, simply because there is no optimal setting for all the conditions.

In this paper, we demonstrate that the delivery of photon energy to the target tissues depends on the multilayered anatomical structure with various optical parameters combinations. 3D volume computational model is built on the magnetic resonance imaging (MRI) of each participant to encompass variations in the thickness and shape of each tissue layer and gyri. The upper and lower bounds of the optical parameters such as absorption and scattering coefficients at various wavelengths are considered for each layer per person. Monte Carlo simulations are performed with all possible combinations of the optical parameters for wavelengths ranging from 650 nm to 1064 nm. Furthermore, different geometrical patterns of radiation sources such as collimated beams and cone beams with different spatial and angular distributions are implemented to find different profiles of photon energy delivery for LLLT on the prefrontal cortex.

II. MATERIALS AND METHODS

A. Human Head Model

3D models of human heads were built based on magnetic resonance images acquired from each human subject. A total of nine subjects participated in this study which has been approved by the internal research board of National Taiwan University. High-resolution T1-weighted structural images were acquired using the 3D-MPRAGE sequence on a 3.0 T Siemens Prisma MRI scanner (Siemens, Erlangen, Germany). A total of 192 contiguous sagittal slices with a voxel size = 0.93 mm × 0.93 mm × 0.93 mm were obtained from each subject. Subsequent image processing was done with MATLAB (The MathWorks, Inc., USA). We used the Statistical Parametric Mapping (SPM12)

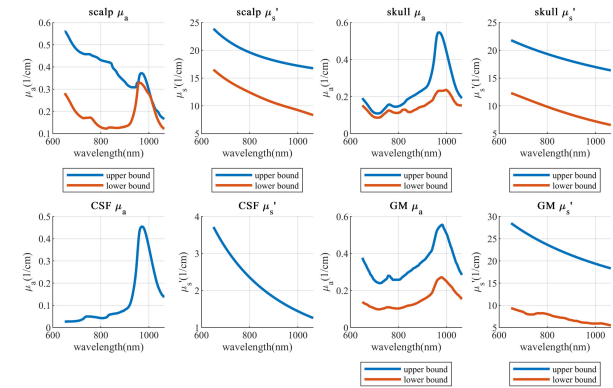


Fig. 1. Optical parameters (i.e., absorption coefficients μ_a and reduced scattering coefficients μ_s') compiled from the literature.

function to segment each voxel into one of five types of tissue including scalp, skull, CSF, GM, and white matter (WM). In addition, we identified regions in the forehead that showed relatively low signal values in the T1 image and classified it as sinus. To locate the area at the scalp surface to be radiated we used the isosurface function to make a surface mesh for the 3D head model and the Mesh2EEG function to find the position of Fp2 in the EEG 10-5 system on the mesh. In all simulations the areas radiated on the scalp surface were set to be centered at the Fp2 position.

B. Optical Parameters

We collected optical parameters (OPs) including the absorption coefficient (μ_a) and the reduced scattering coefficient (μ_s') that are needed to perform Monte Carlo simulations of photon transport from published studies based on *ex-vivo* or intra-operative measurements [15]–[23]. Since one of the aims of this current study was to investigate the optimal wavelength to use in LLLT, only broadband values reported in the literature were adopted and the following descriptions apply to every wavelength considered. In order to encompass the variability in these reported values we set an upper bound and a lower bound for both μ_a and μ_s' of three tissue types including scalp, skull, and GM. The μ_a and μ_s' of the CSF were assumed to be constant according to [24], while the μ_a of WM was set to be half of the GM μ_a , and the μ_s' of WM was set to be three times of the GM μ_s' . The values of OPs are summarized in Fig. 1. There were a total of 65 sets of OPs used in MCX simulations. In one set, the mean OP set, the average of the upper bound and the lower bound values was used. The remaining 64 sets of OPs were determined by choosing either the upper bound or the lower bound value for each of the six OPs summarized in Fig. 1. The Henyey-Greenstein phase function with an anisotropy factor $g = 0.9$ was used for all tissue types. The refractive index of all tissue types was set to be 1.4.

C. Simulation Methods

We used an open-source software package, the Monte Carlo Extreme (MCX), to track the photon propagation trajectory in 3D head models which were built as described in II.A.,

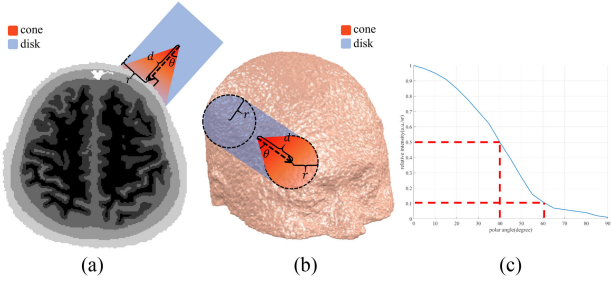


Fig. 2. (a)(b) Schematic diagrams showing the geometry of the cone-beam (red) and collimated-beam (blue) radiation patterns and definitions of parameters r , d , and θ . (c) Angular intensity distribution of an exemplary simulated cone-beam source with the half-angle at half-magnitude (HAHM) = 40°. The maximum angular extent θ of the cone beam is defined as the polar angle where the intensity falls to 10% of its maximum.

and record the photon energy absorbed in each voxel. MCX is parallelized to exploit the high computational efficiency of graphics processing units (GPUs) [25]. Two-hundred million photons were used for each simulation condition to obtain stable results.

Two most commonly used radiation sources were considered in this study including collimated beams generated by lasers and cone beams generated by light-emitting diodes (LEDs). Collimated radiation beams were implemented by the built-in uniform disk source of MCX. The diameter of the disk source was readily assigned in MCX and the direction of radiation was set to be perpendicular to the scalp surface at the Fp2 position. The cone-beam source was implemented as a point source whose radiation direction fell within a cone with a maximum half-angle (θ) as illustrated in Fig. 2(a) and 2(b). Since the exact angular intensity distribution of LEDs depends on specific design of the LED and its packaging, we took the relative angular intensity distribution of an LED available to us (CytonBrite, CytonSys Inc., USA) as shown in Fig. 2(c). The angular extent of the cone, θ , was defined as the angle where the intensity was at 10% of its maximum and equal to about 60° for the exemplary LED. The narrowness of the LED's angular radiation distribution was characterized by the half-angle at half-magnitude (HAHM) which was equal to about 40°. Since the cone-beam source did not emit uniformly over the polar angle, the initial angular direction of a photon packet in MCX simulations was obtained by obtaining the cumulative distribution function (CDF) of the angular intensity distribution, randomly sampling the CDF, and finding the radiation polar angle corresponding to the sampled CDF value [26]. The initial azimuthal angle of a photon packet was randomly sampled from 0– 2π .

D. Data Analysis Methods

The output of MCX simulations was the absorbed photon weight in each voxel. Since the total number of launched photons could represent the total optical power or energy of the source, the power or energy absorbed in each voxel of the head model could be readily obtained. The energy *delivered* to the GM was quantified by summing the photon energy absorbed in all voxels of GM and dividing the sum by μ_a of GM. This parameter has a unit of length (cm) and can be interpreted as the fluence rate

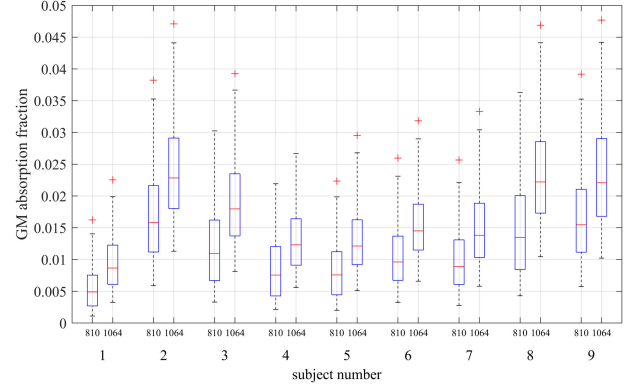


Fig. 3. Fraction of the total source power absorbed in the GM across 64 OP combinations. Obvious variations can be seen among nine subjects with different anatomical structures. Results shown are for wavelength = 810 nm and 1064 nm, and similar trends in OPs and subjects exist in results for other wavelengths.

(unit: $1/\text{cm}^2$) integrated over the volume of the GM. If the target chromophore of LLLT is identified and its absorption coefficient is known, the actual energy absorbed by the target chromophore can be readily calculated.

Note that the two terms “photon power” and “photon energy” were used interchangeably in this manuscript to present results. The term “power” was used specifically for easier interpretation of the results whenever there was a threshold such as the maximum permissible exposure (MPE) with a unit of W/cm^2 or the activation power density with a unit of W/cm^3 .

III. INFLUENCE OF TISSUE OPs, ANATOMICAL STRUCTURE, AND WAVELENGTH

A. Influence of Tissue Optical Parameters (OPs) and Anatomical Structure

Fig. 3 shows the fraction of the source energy that is absorbed in the gray matter (GM) under the radiation of a collimated beam with a diameter of 45 mm. Due to significant deviations in OPs reported in the literature, simulation results using 64 OP combinations showed significant variations, approximately four- to eight-times difference between the highest and the lowest levels for each subject. Therefore, further research on the quantification of OPs of the major tissue layers *in vivo* is imperative. In addition, it can be seen in Fig. 3 that the fraction of the source energy absorbed in the GM varied by up to three times between subjects. The inter-subject variation was estimated by the coefficient of variation (CV) among nine subjects which was about 35%. This simulation result warrants a very important change to the practical implementation of LLLT on the brain. Current LLLT studies/practice use radiations with a fixed power density at the scalp surface. However, according to results shown in Fig. 3, the optical power that is actually absorbed by the GM varies by up to three times. Therefore, an individualized dosage is needed to optimize LLLT effects and prevent overdose due to the hormetic dose-response [27].

Effects of tissue OPs on the photon energy delivered to the brain were investigated by assessing the sensitivity of the energy delivered to the GM to a 2% change in each of the OPs

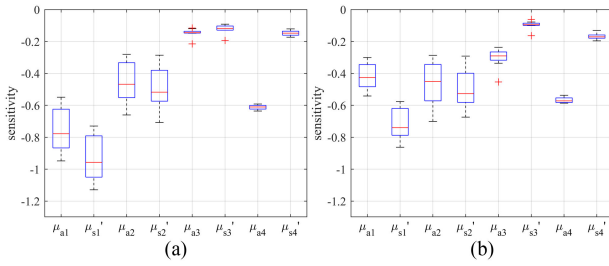


Fig. 4. Sensitivity of the fluence rate integrated over the GM to a 2% change in one of the OPs for (a) wavelength = 810 nm and (b) wavelength = 1064 nm. The box plot shows variations in results due to different anatomical structures of the nine subjects and 13 OP combinations, including the mean OP set and only one of the six OPs being set to the upper or the lower bound value.

including scalp (μ_{a1}, μ_{s1}'), skull (μ_{a2}, μ_{s2}'), CSF (μ_{a3}, μ_{s3}') and GM (μ_{a4}, μ_{s4}') regions. The sensitivity was defined as the fractional change in the GM-integrated fluence rate divided by the fractional change in one OP. The mean OP set was used as the baseline OPs to calculate sensitivity values. To consider effects of different baseline OPs on the sensitivity we changed only one of the six OPs to its upper bound or lower bound value as the baseline OPs. Therefore, a total of 13 OP sets were used to calculate sensitivity values and results are shown in Fig. 4. As expected, increases in both the absorption and the scattering of superficial tissue layers (i.e., scalp, skull, and CSF) increased the attenuation of the incident photon energy, resulting in negative sensitivity values. The results indicate that the scattering of the first tissue layer (scalp) has the strongest influence on the photon energy penetration, followed by the absorption of the scalp and the GM for the wavelength equal to 810 nm and 1064 nm, respectively.

Effects of the anatomical structure on the photon energy delivery efficacy to the brain are difficult to quantify due to the enormous diversity in the curvature and shape of the structures. As a rough estimation, we hypothesized that thicknesses of superficial layers including the scalp, skull and CSF are negatively correlated with the fraction of photon energy penetrating to the GM based on results shown in Fig. 4 and a previous simulation study [11]. We estimated thicknesses of superficial tissue layers under the radiation of the 45-mm-diameter collimated source (Disk1), and calculated Pearson correlation coefficients between the fluence rate integrated over the GM and the thickness of various tissue layers or layer combinations. Fig. 5 shows box plots of correlation coefficients calculated over 64 sets of OPs for the wavelength = 810 nm. Results show that thicknesses of the scalp and the skull are both highly correlated with the energy delivered to the GM, with the total thickness of the scalp, skull, and sinus showing the highest correlation (the average Pearson correlation coefficient = -0.73).

B. Comparison of Photon Energy Delivery Among Wavelengths

As seen in Fig. 3 and reported in the literature, the ability of delivering photon energy to the GM highly depends on tissue OPs and hence also depends on the wavelength of the radiant source. To compare the energy delivered to the GM

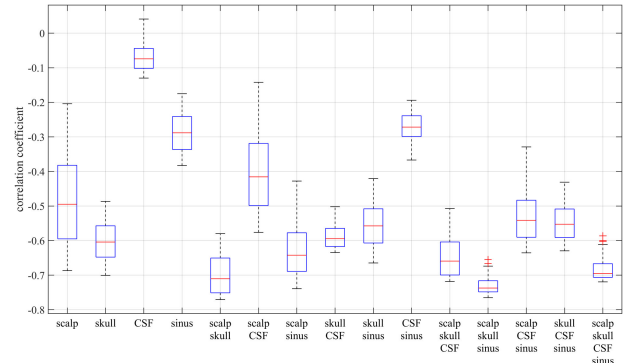


Fig. 5. Correlation coefficients between the fluence rate integrated over the GM and thicknesses of various tissue layers from simulation results of the nine subjects and wavelength = 810 nm. Variations shown in the box plot are due to 64 sets of OPs. The total thickness of the scalp, skull, and sinus shows the strongest negative correlation with a mean correlation coefficient of -0.73.

among wavelengths, the volume-integrated fluence rate in the GM is presented. Fig. 6(a) shows a comparison among radiation wavelengths in the range of 650–1064 nm using the mean OP set, and the similar trend can be seen in results obtained using the rest of the OP combinations. Obvious dips in the energy delivered to the GM can be seen around the 970 nm water absorption peak and toward the short wavelength end where the deoxy-hemoglobin absorption increases rapidly. On the contrary, photon energy delivered to the GM is the highest around 720 nm, 800 nm, and 1064 nm due to local minima of $\mu_a(\lambda)$ as shown in Fig. 2. One result of great interest is the comparison between 810 nm and 1064 nm because these two wavelengths have been frequently used in LLLT on the brain. Fig. 6(b) shows the ratio of the volume-integrated fluence rate between 1064 nm and 810 nm. Although μ_s' of all tissue types are smaller at wavelength = 1064 nm, μ_a of all tissue types except for the scalp are higher at wavelength = 1064 nm due to water absorption. These two factors combined to result in comparable total fluence rates in the GM under radiations with 1064-nm and 810-nm photons. Results based on most OP combinations show that 1064-nm photons are delivered to the GM more efficiently than 810-nm photons. The box plot in Fig. 6(b) shows that there are some OP combinations where the photon energy delivered to the GM is higher at wavelength = 810 nm than 1064 nm. These OP combinations include μ_a of both the scalp and GM at the lower bound and μ_s' of the skull at the upper bound. For μ_a of the scalp, melanin is the major chromophore and absorbs more strongly at 810 nm than at 1064 nm. Therefore, the lower bound scalp μ_a corresponding to lower melanin content attenuates 810-nm photons less strongly. Similarly, hemoglobin absorbs more strongly at 810 nm than at 1064 nm [28], and μ_a of GM at 810 nm is mainly contributed by hemoglobin. Therefore, the lower bound GM μ_a corresponding to lower hemoglobin content facilitates deeper penetration of 810-nm photons to the GM. For skull μ_s' at the upper bound, the value at 810 nm is only 17% higher than that at 1064 nm. Therefore, the upper bound skull μ_s' permits higher 810-nm penetration to the GM relative to 1064-nm than the other skull μ_s' sets.

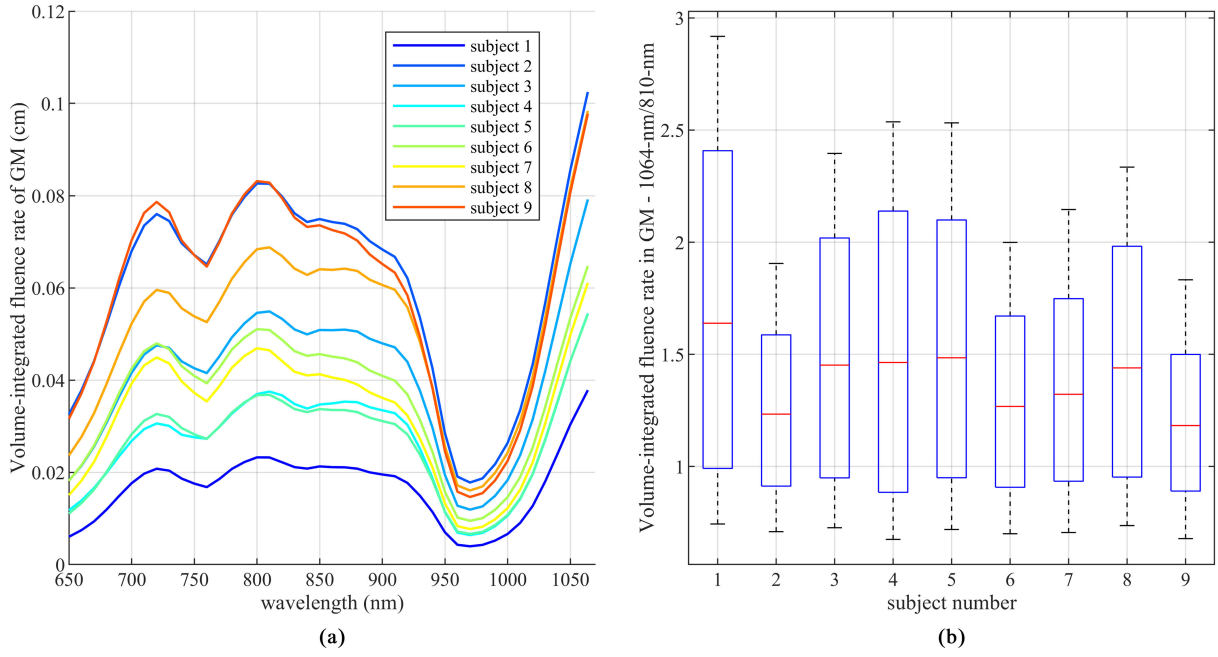


Fig. 6. (a) Comparison of the fluence rate integrated over the GM among nine subjects and wavelengths ranging from 650 nm to 1064 nm. Note that the fluence rate was normalized to the total power of the source. (b) The ratio of the fluence rate integrated over the GM between 1064 nm and 810 nm radiations. In most cases the ratio is larger than one, indicating higher power delivered to the GM under 1064-nm radiation. Variations shown in the box plot are due to 64 sets of OPs.

IV. PHOTON ENERGY DELIVERY EFFICACY OF VARIOUS RADIATION PATTERNS

Firstly, we investigated effects of radiation patterns of both collimated beams and cone beams. Parameters analyzed included the size of the radiated area controlled by the radius (r), and the narrowness of cone beams indicated by the HAHM. Table 1 lists 16 patterns that were investigated. The relative angular intensity distributions of HAMA = 30° and 20° were scaled from the distribution of HAMA = 40° as shown in Fig. 2(c). For a fair comparison between cone-beam and collimated-beam radiations, we set the radiated area by a cone beam at the scalp surface to be approximately the same as that by a given disk source. The distance (d) between the cone-beam source and the scalp surface was determined according to a fixed θ and a predetermined radius (r) of the radiated area. Secondly, to find out the optimal cone-beam pattern for LLLT on the prefrontal cortex, we additionally investigated the optimal distance d to the scalp surface given a fixed power of the source.

To help interpret the simulation results and evaluate the performance, we estimated an activation threshold based on previous experiences of conducting LLLT studies on human subjects. The maximum power density applied on the scalp surface has been 0.4 W/cm² using a 1064-nm laser with a beam diameter of 4.5 cm (the total power is about 6.36 W assuming a uniform distribution), and enhancing effects on cognitive functions have been observed in most of the healthy participants. Assuming this radiation power is sufficient to activate the whole GM region underneath the radiated area, and according to Fig. 7(d) that most of the GM region under the radiated area has a volumetric power density of at least 0.1 mW/cm³ due to the total radiation power of 1 W, we estimated an activation threshold to be 0.6 mW/cm³.

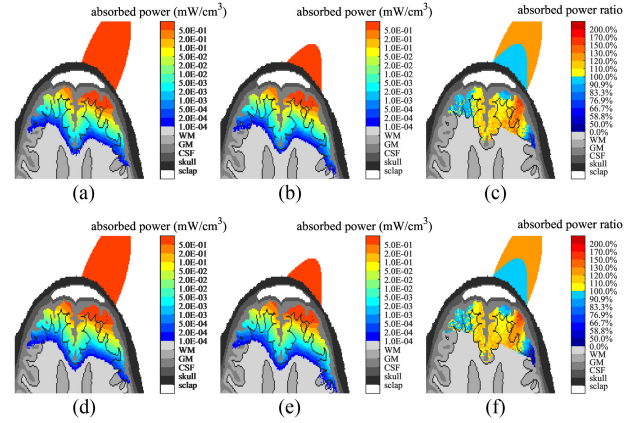


Fig. 7. Cross-sectional views of the distribution of the absorbed power per unit volume in the head model of subject #6 under (a)-(d) collimated-beam (Disk1), and (b)-(e) cone-beam (Cone1) radiations with a wavelength of 810 nm [(a)-(c)] and 1064 nm [(d)-(f)]. The total power of the sources was the same at 1W. The ratios of the absorbed volumetric power density between the collimated beam and the cone beam are shown in (c) and (f) for the wavelength of 810 nm and 1064 nm, respectively. Videos of full three-dimensional stacks can be found in Supplementary Materials.

A. Comparison Between Collimated Beams and Cone Beams

Fig. 7(a) and 7(b) show distributions of the absorbed photon power per unit volume in the head model of subject #6 under the collimated-beam (Disk1) and cone-beam (Cone1) radiation for wavelength = 810 nm, respectively. Note that the radiated area was approximately the same under the two patterns, and the total power of the two patterns was also set to be the same at 1 W. Therefore, we can see effects of the spatial and angular distributions of incident photons. It is obvious and as expected

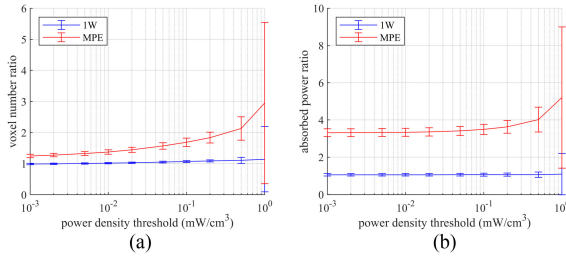


Fig. 8. Comparison of photon energy delivery metrics between collimated-beam and cone-beam radiations showing values of the Disk1 source divided by values of the Cone1 source. (a) The number of active voxels against the activation threshold, and (b) the total power absorbed in active voxels against the threshold. The total source power was set to 1 W for the two types of radiation (blue lines), and set to be their corresponding maximum limited by MPE (red lines). Error bars indicate standard deviations among nine subjects and 64 sets of OPs.

that the photon energy decayed exponentially with the depth into the tissue. To better compare and visualize differences between the two types of radiation sources, the ratio of the absorbed power density between Disk1 and Cone1 is shown in Fig. 7(c). It can be seen that the Cone1 source generates more focused energy distribution near its optical axis and decays more rapidly toward the edges in the plane transverse to the optical axis of the source. In other words, the collimated beam with approximately uniform intensity distribution (Disk1) illuminates the head more uniformly in the transverse plane. Similar results are shown in Fig. 7(d)-7(f) for the wavelength of 1064 nm.

To quantitatively compare the performance of the two types of sources in delivering photon energy to the GM, blue curves in Fig. 8 show ratios of two performance metrics between Disk1 and Cone1 with wavelength = 810 nm and the same total power of 1 W. Error bars indicate variations among nine subjects and 64 OP sets. It is interesting to note that when the threshold changes from 0.01 mW/cm³ to 1 mW/cm³, the ratio of the number of active voxels [Fig. 8(a)] increases while the ratio of the total energy absorbed in active voxels [Fig. 8(b)] remains constant. This can be explained as follows: in this threshold range Disk1 has a more uniform energy distribution, which results in more active voxels than Cone1 when the threshold is higher. However, since the photon energy under Cone1 is more concentrated, the two patterns have similar total energy in active voxels.

Next we evaluated which radiation pattern listed in Table I was the best according to the same performance metrics. Since more energy entering the tissue generally results in higher energy deposit in the brain, the total power of each radiation pattern was set at its corresponding maximum that was allowed by the MPE value at the scalp surface [29]. The MPE is 332 mW/cm² for 810 nm and 1 W/cm² for 1064 nm photons. How to estimate the maximum power density at the scalp surface for a cone-beam radiation pattern is explained in Supplementary Materials. Red lines in Fig. 8(a) and 8(b) show that Disk1 outperforms Cone1 at all threshold levels. Fig. 9(a)-9(c) show correlations between the MPE-limited total power of each radiation pattern and its ability to deliver the photon energy to the GM at the wavelength of 810 nm, and Fig. 9(d)-9(f) show the same results at the wavelength of 1064 nm. All three performance metrics show

TABLE I
GEOMETRICAL PARAMETERS OF RADIATION PATTERNS INVESTIGATED

r (mm)	Collimated-beam patterns	Cone-beam patterns		
		HAHM=20°	HAHM=30°	HAHM=40°
22.5	Disk1	Cone1, $d=37.3$ mm	Cone2, $d=20.2$ mm	Cone3, $d=11.8$ mm
20	Disk2	Cone4, $d=33.3$ mm	Cone5, $d=17.7$ mm	Cone6, $d=9.7$ mm
15	Disk3	Cone7, $d=25.7$ mm	Cone8, $d=13.8$ mm	Cone9, $d=7.1$ mm
10	Disk4	Cone10, $d=18$ mm	Cone11, $d=10$ mm	Cone12, $d=5.3$ mm

Names of simulated collimated-beam and cone-beam patterns and their properties including the radius of the radiated area on the scalp surface (r), the HAHM, and the average distance to the scalp surface (d).

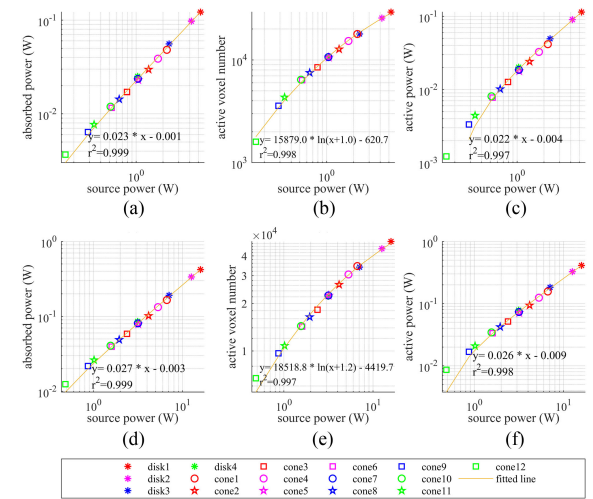


Fig. 9. Correlations between three photon energy delivery efficacy metrics and the MPE-restricted total power of the 16 radiation patterns listed in Table I: (a)-(d) total power absorbed in GM, (b)-(e) number of voxels above a threshold of 0.6 mW/cm³, and (c)-(f) total power absorbed in voxels above the threshold. Results shown are based on the anatomical model of subject #6 and the wavelength of 810 nm [(a)-(c)] and 1064 nm [(d)-(f)], respectively.

high positive correlations and are representative of those based on other subjects' head structures and wavelengths. Therefore, the total energy delivered to the GM is dominated by the total energy emitted by the 16 radiation patterns. The spatial and angular intensity distributions of the radiation beams investigated in this study are not as important. Although the threshold was chosen to be 0.6 mW/cm³ as an example, the general trend was similar when other threshold values were used. In conclusion, the results indicate that collimated beams are better than cone beams because the former have a more uniform spatial distribution of energy. Thus, higher total power can be used given approximately the same radiated area. The results also suggest that a larger beam size is advantageous to activate a larger region of the brain.

B. Comparison Among Cone Beams With the Same Power

Results in Figs. 8 and 9 show that collimated beams, typically generated by lasers, are more effective than cone beams because

TABLE II
GEOMETRICAL PARAMETERS OF CONE-BEAM PATTERNS WITH THE SAME SOURCE POWER = 1W

HAHM	Pattern name and distance d (mm)		
20°	Cone13, $d=25$	Cone4, $d=33$	Cone1, $d=37$
30°	Cone14, $d=17$		
40°	Cone15, $d=13$	Cone16, $d=17$	Cone17, $d=24$

Cone13, Cone14, and Cone15 are at locations that result in the maximum power density at the scalp surface equal to the MPE value of 332 mW/cm² for wavelength = 810 nm and HAHM = 20°, 30° and 40°, respectively.

a more uniform intensity distribution can be generated and a higher total power can be employed without exceeding the MPE level at the scalp surface. In practice however, LEDs are a preferred choice to lasers because they are much cheaper and less hazardous than lasers. Therefore, we investigated which cone beam is the most effective to deliver photon energy to the brain. We considered three cone-beam sources with an identical radiant power of 1 W at a wavelength of 810 nm, and different angular distributions of HAHM being equal to 20°, 30° and 40°, respectively. The location of the cone-beam sources was controlled by the parameter d . The shortest distance d to the scalp was determined for each of the three sources based on the MPE, and the three corresponding patterns were named Cone13, Cone14 and Cone15, respectively. Cone15 (HAHM = 40°) is located at $d = 13$ mm where the maximum power density at the scalp surface reaches the MPE. Therefore, the cone-beam patterns with HAHM = 40° listed in Table I cannot be used and we added two locations at $d = 17$ mm (Cone16) and $d = 24$ mm (Cone17) to investigate the influence of the distance between the scalp and the cone source with HAHM = 40°. Cone-beam patterns analyzed and compared are listed in Table II.

Fig. 10(a) and 10(b) show comparisons of photon energy delivery efficacy metrics between the same cone-beam source with HAHM = 20° placed at various distances (d) to the scalp surface. Fig. 10(c) and 10(d) show similar comparisons for the cone-beam source with HAHM = 40°. Fig. 10(b) and 10(d) show that the energy absorbed in active voxels are the highest when the source is located the closest to the scalp (Cone13 and Cone15, respectively), no matter which activation threshold value is chosen. Fig. 10(a) and 10(c) show that numbers of active voxels resulting from the same cone-beam source located at various distances are comparable for the threshold of 0.6 mW/cm³. However, for higher threshold values the patterns with the shortest d activate the most voxels. Overall, cone-beam sources are recommended to be placed as close to the scalp as possible, up to the separation which ensures the safety of the radiated scalp.

Fig. 10(e) and 10(f) show the relative performance between Cone13, Cone14 and Cone15. Cone13, which has the narrowest angular distribution among the three patterns investigated, results in more energy absorbed in active voxels than the other two cone-beam sources for all threshold levels and more active voxels for an activation threshold of 0.6 mW/cm³ or above. The results suggest that given the same source power a cone-beam source with a narrower angular intensity distribution is preferred,

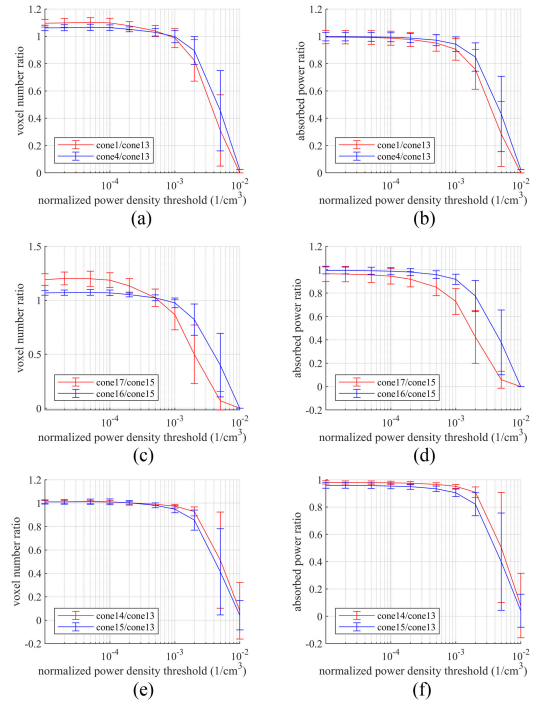


Fig. 10. Comparison of (a)(c) the number of active voxels, and (b)(d) the total power absorbed in active voxels between the same cone-beam source located at different distances d to the scalp surface; (a)(b) HAHM = 20° source and (c)(d) HAHM = 40° source. Results show that for normalized thresholds of at least 6×10^{-4} the sources located the closest to the scalp surface perform the best. Parts (e) and (f) further compare the photon delivery efficacy metrics between cone-beam sources with different HAHM of 20° (Cone13), 30° (Cone14) and 40° (Cone15), all located as close to the scalp surface as permitted by the MPE value of 332 mW/cm². Error bars indicate standard deviations among nine subjects.

especially under the condition of a higher activation threshold than the currently assumed 0.6 mW/cm³.

C. Effects of Reduced Cone-Beam Powers

The above analyses were based on the assumption of a fixed source power of 1 W. In practice, LED sources with lower power levels are more available. To illustrate the effect of a lower radiant power of light sources on the efficacy of delivering energy to the GM, we simulated two more cone-beam sources with HAHM = 40° and a radiant power of 0.7 W and 0.5 W, respectively. The closest distance to the scalp surface was calculated to be about 11 mm and 9 mm, respectively. Performance metrics relative to the HAHM = 40° and 1 W source (Cone15) are presented in Fig. 11(a) and 11(b). While Fig. 11(a) shows that the number of active voxels above a threshold of 0.6 mW/cm³ are about 0.7 and 0.5 times of those achieved with Cone15, Fig. 11(b) shows that the total power absorbed in active voxels are only 0.6 and 0.36 times of those achieved with Cone15, respectively. Moreover, both of the relative performance metrics decrease rapidly with increased activation threshold. The relative performance metrics obtained from simulations of the HAHM = 20° sources are a few percent higher than those from the HAHM = 40° sources (data not shown). The results suggest that cone-beam sources with sufficiently high power levels are necessary for LLLT on

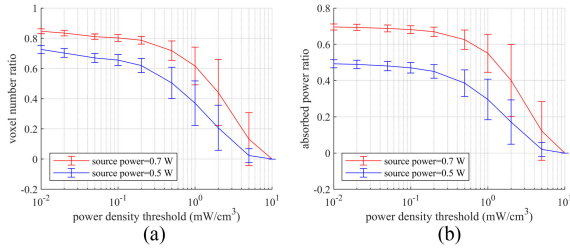


Fig. 11. Effects of a lower source power of 0.7 W or 0.5 W on the photon delivery efficacy metrics of HAHM = 40° cone-beam source. Results show ratios of (a) the number of active voxels and (b) the total power absorbed in active voxels between a lower power source and the source with power = 1 W (Cone15). All sources are located as close to the scalp surface as allowed by the MPE. Error bars indicate standard deviations among nine subjects.

the prefrontal cortex. The exact power required is dependent on the threshold which is an important topic of further research.

V. DISCUSSION AND CONCLUSION

In order to optimize beneficial effects of LLLT on the brain cortex, it is necessary to model the photon energy distribution in the brain and quantify the volumetric fluence rate which has a unit of optical power per unit volume as shown in Fig. 7. Simulation results of collimated-beam radiation with a beam diameter of 45 mm show that about 0.3% to 3% of the total light source power reaches the GM, which is in agreement with previous studies [11]. However, precise quantification of the fluence rate in the GM due to external irradiation is not feasible because of the high variability in tissue OPs reported in the literature. In addition, variability in the anatomical structure between individuals needs to be addressed. The results call for the development of new methods to determine *in vivo* the fraction of the source radiation power that actually reaches the GM for each human recipient of LLLT. Further research and development have been ongoing in our group to address this issue. We propose to measure diffuse reflectance spectra from multiple source-detector separations on the scalp surface and use Monte Carlo modeling to find out the correlation between measured spectra and the fraction of source energy delivered to the brain. Diffuse reflectance techniques are well suited for this purpose because they are cost-effective and compatible with Monte Carlo modeling of photon propagation in tissue.

Despite the high variability in the simulation results of the absolute fluence rate in the GM, comparative studies on the optimization of radiation parameters for LLLT are still valuable and results are consistent across OPs and anatomical structures. We investigated influences of the wavelength and the angular and spatial intensity distributions of the radiation source on the efficacy of delivering photon energy to the GM given the currently available OPs of tissue layers in the head. Simulation results of the volume-integrated fluence rate in the GM revealed maxima around 720, 800, and 1064 nm, which are local minima of tissue absorption coefficients. The same trend can be observed across the nine subjects included in the current study, as shown in Fig. 6(a). For the comparison between 810 nm and 1064 nm which are the most commonly used wavelengths in LLLT on the brain, 1064-nm photons generally have a deeper penetration than

810-nm photons due to the smaller scattering effect. However, in some situations the penetration of the two wavelengths is similar depending on the absorption coefficients of that individual. For individuals with lighter skin and/or lower hemoglobin content in the brain, 810-nm photons could achieve deeper energy delivery than 1064-nm photons. We have been developing methods to quantify the OPs of major tissue layers in the head for each individual *in vivo* to verify the OPs used in the simulations.

For a comprehensive comparison of radiation sources we analyzed the following two scenarios. In the first scenario we compared the photon energy delivery efficacy among various radiation patterns by assuming that the total power of each pattern is limited by its maximum power density at the scalp surface being equal to the MPE. Collimated beams which are typically generated by lasers performed better than diverging beams due to a more uniform spatial distribution of the irradiance and therefore a higher total power can be used. In the second scenario we attempted to find optimal conditions of using LEDs for LLLT by comparing the photon energy delivery performance among cone-beam radiation patterns given a fixed source power. Attributes analyzed included the narrowness of the angular intensity distribution which is an attribute of the source, and the distance between the scalp surface and the source which can be freely adjusted by the experimenter or device designer. Simulation results recommend to use cone-beam sources with a narrower angular intensity distribution and placed as close to the tissue as permitted for the safety of the tissue. Arranging cone-beam sources in arrays is viable to increase the total power impinging on the scalp surface and activate larger areas of the brain. However, for targeting a broad region with a single light source, collimated beams would be preferred because evenly distributed energy could be better delivered.

The near-infrared light within the range of 700–1100 nm for LLLT generally does not induce much heat. By following the protocol in [12], the measured increase in temperature on the surface of the scalp at the laser treatment spot was within one degree Celsius. In addition, the human body regulates the body temperature to keep it at a constant level especially in the inner organs and the brain. Therefore, all the tissues under the skull are not expected to have any temperature difference caused by the radiation of photons at such a low power density range (i.e., 250 mW/cm² in [12]).

We would like to point out that this study focuses on the energy delivery through continuous-wave radiations, but how the tissues react to photons with a certain wavelength or pulse duration is not covered. Different wavelengths of photons have different influences on the cells. For example, in [30] 750 nm and 950 nm photons show inhibitory modulation on the CCO activity, while 810 nm and 1064 nm photons show excitatory modulation on the CCO [3], [10], [12]. The excitatory modulation on the CCO activity increases the efficiency in ATP generation. Synaptic activities and the neuroplasticity consume a lot of ATPs. If the ATP generation efficiency slows down or is compromised, many issues are induced such as cognitive function impairments, dementia, etc. [10], [12]. On the other hand, the inhibitory wavelengths such as 750 nm and 950 nm reduce mitochondrial respiration and the mitochondrial membrane potential. These reactions result in attenuating both the mitochondrial superoxide

production and neuronal deaths following oxygen and glucose deprivations. The inhibitory modulation is a potential therapy for cerebral reperfusion injury as evidenced by a study using a rat model of global brain ischemia [30]. The overall effect on the brain tissue would need to consider the tissue response in order to adopt the LLLT in practice.

Quantification of the absolute energy delivered to the brain relies on accurate quantifications of the tissue OPs which have not been established. Nonetheless, the preliminary simulation results obtained in the study provide valuable information for the implementation and optimization of LLLT on the brain. The fractional power delivered to the GM is estimated to vary within an order of magnitude depending on OPs and the head structure of the individual. If more precise control of the LLLT dosage is required, effects of OPs and anatomical structure need to be considered for each individual.

REFERENCES

- [1] J. T. Hashmi *et al.*, "Role of low-level laser therapy in neurorehabilitation," *PM R : J. Inj., Function, Rehabil.*, vol. 2, no. 12 Suppl 2, pp. S292–S305, 2010.
- [2] J. C. Rojas and F. Gonzalez-Lima, "Neurological and psychological applications of transcranial lasers and LEDs," *Biochem. Pharmacol.*, vol. 86, no. 4, pp. 447–457, Aug. 15, 2013.
- [3] X. Wang, F. Tian, S. S. Soni, F. Gonzalez-Lima, and H. Liu, "Interplay between up-regulation of cytochrome-c-oxidase and hemoglobin oxygenation induced by near-infrared laser," *Sci. Rep.*, vol. 6, Aug. 3, 2016, Art. no. 30540.
- [4] S. G. Disner, C. G. Beevers, and F. Gonzalez-Lima, "Transcranial laser stimulation as neuroenhancement for attention bias modification in adults with elevated depression symptoms," *Brain Stimul.*, vol. 9, no. 5, pp. 780–787, Sep./Oct. 2016.
- [5] J. Hwang, D. M. Castelli, and F. Gonzalez-Lima, "Cognitive enhancement by transcranial laser stimulation and acute aerobic exercise," *Lasers Med. Sci.*, vol. 31, no. 6, pp. 1151–1160, Aug. 2016.
- [6] F. Tian, S. N. Hase, F. Gonzalez-Lima, and H. Liu, "Transcranial laser stimulation improves human cerebral oxygenation," *Lasers Surg. Med.*, vol. 48, no. 4, pp. 343–349, Apr. 2016.
- [7] N. J. Blanco, W. T. Maddox, and F. Gonzalez-Lima, "Improving executive function using transcranial infrared laser stimulation," *J. Neuropsychol.*, vol. 11, no. 1, pp. 14–25, Mar. 2017.
- [8] F. Gonzalez-Lima and D. W. Barrett, "Augmentation of cognitive brain functions with transcranial lasers," *Front. Syst. Neurosci.*, vol. 8, pp. 36, 2014.
- [9] S. Chen *et al.*, "Near-infrared deep brain stimulation via upconversion nanoparticle-mediated optogenetics," *Science*, vol. 359, no. 6376, pp. 679–684, Feb. 9, 2018.
- [10] D. W. Barrett and F. Gonzalez-Lima, "Transcranial infrared laser stimulation produces beneficial cognitive and emotional effects in humans," *Neuroscience*, vol. 230, pp. 13–23, Jan. 29, 2013.
- [11] P. Cassano *et al.*, "Selective photobiomodulation for emotion regulation: Model-based dosimetry study," *Neurophotonics*, vol. 6, no. 1, Jan. 2019, Art. no. 015004.
- [12] E. Vargas *et al.*, "Beneficial neurocognitive effects of transcranial laser in older adults," *Lasers Med Sci.*, vol. 32, no. 5, pp. 1153–1162, Jul. 2017.
- [13] P. Wang and T. Li, "Which wavelength is optimal for transcranial low-level laser stimulation?" *J. Biophotonics*, vol. 12, no. 2, Feb. 2019, Art. no. e201800173.
- [14] A. Pitzschke *et al.*, "Red and NIR light dosimetry in the human deep brain," *Phys. Med. Biol.*, vol. 60, no. 7, pp. 2921–2937, Apr. 7, 2015.
- [15] A. N. Bashkatov, E. A. Genina, V. I. Kochubey, and V. V. Tuchin, "Optical properties of human skin, subcutaneous and mucous tissues in the wavelength range from 400 to 2000 nm," *J. Phys. D-Appl. Phys.*, vol. 38, no. 15, pp. 2543–2555, Aug. 2005.
- [16] C. R. Simpson, M. Kohl, M. Essnenpreis, and M. Cope, "Near-infrared optical properties of ex vivo human skin and subcutaneous tissues measured using the monte carlo inversion technique," *Phys. Med. Biol.*, vol. 43, no. 9, pp. 2465–2478, Sep. 1998.
- [17] E. K. Chan *et al.*, "Effects of compression on soft tissue optical properties," *IEEE J. Sel. Topics Quantum Electron.*, vol. 2, no. 4, pp. 943–950, Dec. 1996.
- [18] N. Okui and E. Okada, "Wavelength dependence of crosstalk in dual-wavelength measurement of oxy- and deoxy-hemoglobin," *J. Biomed. Opt.*, vol. 10, no. 1, Jan./Feb. 2005, Art. no. 11015.
- [19] A. N. Bashkatov, E. A. Genina, V. I. Kochubey, and V. V. Tuchin, "Optical properties of human cranial bone in the spectral range from 800 to 2000 nm," in *Proc. SPIE*, 2006, Art. no. 616310.
- [20] F. Bevilacqua *et al.*, "In vivo local determination of tissue optical properties: Applications to human brain," *Appl. Opt.*, vol. 38, no. 22, pp. 4939–4950, Aug. 1, 1999.
- [21] A. Farina *et al.*, "In-vivo multilaboratory investigation of the optical properties of the human head," *Biomed. Opt. Exp.*, vol. 6, no. 7, pp. 2609–2623, Jul. 2015.
- [22] P. van der Zee, M. Essenpreis, and D. T. Delpy, "Optical properties of brain tissue," in *Proc. SPIE*, 1993, pp. 454–465.
- [23] A. N. Yaroslavsky *et al.*, "Optical properties of selected native and coagulated human brain tissues in vitro in the visible and near infrared spectral range," *Phys. Med. Biol.*, vol. 47, no. 12, pp. 2059–2073, Jun. 21, 2002.
- [24] E. Okada and D. T. Delpy, "Near-infrared light propagation in an adult head model. I. Modeling of low-level scattering in the cerebrospinal fluid layer," *Appl. Opt.*, vol. 42, no. 16, pp. 2906–2914, Jun. 1, 2003.
- [25] Q. Fang and D. A. Boas, "Monte carlo simulation of photon migration in 3D turbid media accelerated by graphics processing units," *Opt. Exp.*, vol. 17, no. 22, pp. 20178–20190, Oct. 26, 2009.
- [26] C. Kortun, Y. R. Hijazi, and D. Arifler, "Combined monte carlo and finite-difference time-domain modeling for biophotonic analysis: Implications on reflectance-based diagnosis of epithelial precancer," *J. Biomed. Opt.*, vol. 13, no. 3, May/Jun. 2008, Art. no. 034014.
- [27] Y. Y. Huang, A. C. Chen, J. D. Carroll, and M. R. Hamblin, "Biphasic dose response in low level light therapy," *Dose Response*, vol. 7, no. 4, pp. 358–383, Sep. 2009.
- [28] M. Friebel and M. Meinke, "Determination of the complex refractive index of highly concentrated hemoglobin solutions using transmittance and reflectance measurements," *J. Biomed. Opt.*, vol. 10, no. 6, Nov./Dec. 2005, Art. no. 064019.
- [29] American National Standard for Safe Use of Lasers, ANSI standard Z136.1, 2014.
- [30] T. H. Sanderson *et al.*, "Inhibitory modulation of cytochrome c oxidase activity with specific near-infrared light wavelengths attenuates brain ischemia/reperfusion injury," *Sci. Rep.*, vol. 8, no. 1, Feb. 22, 2018, Art. no. 3481.



Li-Da Huang (Senior Member, IEEE) received the Ph.D. degree in computer sciences from the University of Texas, Austin, TX, USA. He has authored or coauthored more than 30 papers and patents. Several papers are regarded as pioneer work in low-level light therapy (LLLT), EEG study for photo-bio-modulation (PBM), design for manufacturing in OPC-friendly routing, antenna effects in routing, and redundant via insertion, which was nominated as the most influential paper in the past decade in ASPDAC 2015. His research interests include neural sciences, artificial intelligence, circuit design, design automation, computer vision, signal processing, brain modeling, cognitive function enhancement, aging process, and bio-modulation. He is a Member of the Upsilon-Pi-Epsilon, International Honor Society for the computing and information disciplines.



Tzu-Chia Kao received the B.S. degree in 2018 in electrical engineering from National Taiwan University, Taipei, Taiwan, where he is currently working toward the M.S. degree in biomedical electronics and bioinformatics. Since 2018, he has been a Graduate Research Assistant with Biomedical Spectrum and Optical Imaging Laboratory, National Taiwan University. His research interests include Monte Carlo simulations of the photon-tissue interaction and diffusion reflectance spectroscopy.



Kung-Bin Sung was born in Taipei, Taiwan. He received the B.S. degree in electrical engineering from National Taiwan University, Taipei, in 1996, and the M.S. and Ph.D. degrees, in 1999 and 2003, respectively. After finishing two years of mandatory military service, he joined with The University of Texas at Austin, Austin, TX, USA, in 1998, majoring in biomedical engineering. His main research project as a Student was developing a fiber-optic confocal microscope to obtain images of epithelial cells *in vivo* for the diagnosis of early cancer and precancerous lesions. In 2003, he joined Intel Corporation as a Research Scientist, and collaborated with researchers with the Fred Hutchinson Cancer Research Center, Seattle, WA, USA, working on research projects related to surface-enhanced Raman spectroscopy. Since Jul. 2006, he has been a Faculty Member with National Taiwan University, where he is currently an Associate Professor. His current research interests include the development and applications of optical spectroscopy and microscopy techniques for the diagnosis of early cancer and precancerous lesions, continuous monitoring of physiological parameters, and the improvement of health through low-level light therapy.



Jacob A. Abraham (Fellow, IEEE) received the bachelor's degree in electrical engineering from the University of Kerala, India, in 1970, and the M.S. degree in electrical engineering and the Ph.D. degree in electrical engineering and computer science from Stanford University, Stanford, CA, USA, in 1971 and 1974, respectively. From 1975 to 1988, he was with the Faculty, University of Illinois, Urbana-Champaign, IL, USA.

He is currently a Professor with the Department of Electrical and Computer Engineering, The University of Texas at Austin, Austin, TX, USA. He is also the Director with the Computer Engineering Research Center and holds the Cockrell Family Regents Chair in engineering. He has more than 300 publications, and has been included in a list of the most cited researchers in the world. He is the Principal Investigator of several contracts and grants in his research fields, and a Consultant to industry and government on testing and fault-tolerant computing. He has supervised more than 60 Ph.D. dissertations. He is particularly proud of the accomplishments of his students, many of whom occupy senior positions in academia and industry. His research interests include VLSI design and test, formal verification, and fault-tolerant computing.

He was an Associate Editor of several IEEE transactions, and the Chair of the IEEE Computer Society Technical Committee on Fault-Tolerant Computing. He has been elected the Fellow of the ACM, and was the recipient of the 2005 IEEE Emanuel R. Piore Award.